JMEPEG (2020) 29:5184–5194
https://doi.org/10.1007/s11665-020-05025-z

1059-9495/$19.00

Surface Integrity of TA19 Notched Simulated Blades with Laser Shock Peening and Its Effect on Fatigue Strength

Junfeng Wu, Zhigang Che, Shikun Zou, Ziwen Cao, and Rujian Sun

(Submitted April 7, 2020; in revised form June 20, 2020; published online August 17, 2020)

To reveal the fatigue strengthening mechanism of TA19 notched simulated blades with laser shock peening (LSP), surface integrity and fatigue strength were investigated. The surface morphology, residual stress, near-surface microstructure, fatigue strength and fatigue fracture morphology were analyzed by surface profiler, x-ray diffraction (XRD), transmission electron microscopy (TEM), QRG-100 servo-hydraulic fatigue test machine and scanning electron microscope (SEM). Results indicated that LSP induced surface micro-dents plastic deformations with a few microns in depth, surface compressive residual stresses and surface nano-grains of TA19 notched simulated blades. Compared with the as-received material, fatigue strengths of TA19 notched simulated blades were improved by 162% for LSP-1 and 218% for LSP-3. In addition, fatigue crack initiation (FCI) locations reduced after LSP, fatigue crack growth (FCG) rate decreased after LSP, and secondary cracks were observed in the FCI and FCG regions of fatigue fracture morphologies after LSP. Fatigue strengthening mechanism of TA19 notched simulated blades with LSP was compressive residual stresses and refined grains. Results could be beneficial to the application of LSP process in civil engines blades.

Keywords compressive residual stresses, fatigue strengthening mechanism, laser shock peening (LSP), refined grains, TA19 notched simulated blades

1. Introduction

TA19 alloy (also named as Ti-6Al-2Sn-4Zr-2Mo for ASTM) is a near-α titanium alloy and widely used in civil engines as integral disks and blades because of its great mechanical property (Ref 1-3). However, the blade leading edge experiences the foreign object and is subjected to the foreign object damage (FOD) during the aircraft takeoff and landing (Ref 4). The velocities of these objects may reach 500 m/s, which cause the stress concentrations or the failure sources at the leading edge of the blades. Then, these cause the rapid fracture of blades (Ref 5, 6). In addition, the titanium alloy is very sensitive to the FOD notch. As a result, the FOD notch has been identified as one of the main factors limiting the fatigue lives of civil engine blades.

In recent years, advanced surface treatments, such as laser shock peening (LSP), have been used to improve the fatigue crack growth (FCG) resistance of the critical components (Ref 7, 8). Compared with the traditional shot peening, LSP induces much deeper compressive residual stress layers at the leading edge of the blade. Then, it improves the damage tolerance capability of the blade (Ref 9).

It is very important for the critical components to understand the effect of the FOD notch on the fatigue performance (Ref 10, 11). It has been reported that fatigue performances of titanium alloy notched simulated blades were improved by LSP in the complex residual stress field (Ref 4, 12). Ruschau et al. (Ref 13, 14) investigated the FCG characteristics of TC4 notched simulated blades without and with LSP under the low (R = 0.1) and high (R = 0.8) stress ratios. Compared with the as-received material, the improvements of the FCG rate of TC4 notched simulated blades with LSP were slight under the high-cycle fatigue (HCF) test condition and significant under the low-cycle fatigue (LCF) test condition. Lin et al. (Ref 4) experimentally and numerically analyzed the FCG behavior of TC4 notched simulated blades with LSP prior to the FOD notch. For TC4 notched simulated blades with LSP prior to the FOD notch, the improvement of the FCG behavior under the LCF condition was more obvious than that under the HCF and LCF + HCF conditions. Compared with the as-received material, the fatigue crack initiation (FCI) was delayed by LSP and the FCG rate was reduced by LSP. Spanrad et al. (Ref 15) discussed the FOD damage process of TC4 notched aerofoil samples and the effect of LSP on their fatigue performances under the LCF, HCF and LCF + HCF conditions. Compared with the as-received material, the onset of the FCG of TC4 notched aerofoil samples was delayed by LSP under the LCF and LCF + HCF conditions. It indicated that LSP effectively improved the anti-FOD fatigue performance of TC4 notched aerofoil samples. The above studies mainly discussed the anti-FOD fatigue performance of TC4 notched simulated blades with and without LSP. TC4 alloy is a two-phase titanium alloy with α + β phases, which has the advantages of low density, high stiffness and strength to weight radios. Unlike the TC4 alloy, TA19 alloy is a near-α titanium alloy, which has the advantages of lightweight and superior

Junfeng Wu, Zhigang Che, Shikun Zou, Ziwen Cao, and **Rujian Sun**, Science and Technology on Power Beam Processes Laboratory, AVIC Manufacturing Technology Institute, Beijing 100024, People's Republic of China. Contact e-mail: wjf88813@163.com.

creep properties at elevated temperatures up to 600°. Therefore, it has been used in jet engines as compressor disks and blades. However, the leading edges of TA19 civil engines blades were also vulnerable to the FOD damage during the aircraft takeoff. Therefore, it is very necessary to study the anti-FOD fatigue performance and its fatigue strengthening mechanism at the leading edge of TA19 notched simulated blades with LSP.

Luo et al. (Ref 16) studied the fatigue strength and its crucial effect factors of TC4 alloy treated by LSP and subsequently exposing to the FOD damage. It indicated that combined residual stresses induced by LSP and the FOD impact played a role on the fatigue strength. Zabeen et al. (Ref 12, 17) investigated the residual stress distributions at the leading edge of TC4 aerofoil samples treated by LSP and prior to the FOD damage and examined how the non-uniform gradient residual stress profiles varied as a function of the FCG under the HCF and LCF + HCF conditions. The results indicated that maximum compressive residual stress values were obtained beneath the FOD notch. In addition, compressive residual stresses values for the 0° impact condition were larger than those for the 45° impact condition, which owed to the larger depth of the FOD notch for the 0° impact condition. Wu et al. (Ref 9) designed the TC17 notched simulators approximating the cross section of blades leading edge with the FOD notch and discussed the anti-FOD fatigue performance after LSP. Compared with the as-received material, fatigue strength of TC17 notched simulators with LSP was increased by 55.6%. No previous works investigated the fatigue strengthening mechanism of TA19 notched simulated blades with LSP through macro- and micro-fatigue fracture morphologies. Compared with TC4 and TC17 alloy, mechanical properties of TA19 alloy were obviously different. Therefore, it was necessary to study the fatigue strength and fatigue strengthening mechanism of TA19 notched simulated blades with and without LSP. It had a very important research significance for the application of LSP process in civil engine blades.

The paper comprehensively considered the surface integrity and its effect on the fatigue strength and fatigue fracture morphology at the leading edge of TA19 notched simulated blades with and without LSP. The surface integrity included the surface morphology, surface residual stress and near-surface microstructure. Furthermore, fatigue strengthening mechanism of TA19 notched simulated blades with LSP was revealed through the fatigue fracture morphology.

2. Experimental Methods and Measured Analysis

2.1 Material and Samples

TA19 alloy was used as the experimental material. Its microstructure consists of primary α phase in conjunction with lamellar $\alpha + \beta$ colonies, as shown in Fig. 1. Its chemical compositions are presented in Table 1. Its heat treatment process was the double annealing with a 970 °C/1 h air cooled and a 595 °C/8 h air cooled. Its mechanical properties at room temperature were as follows: an ultimate tensile strength of 1030 MPa and an elongation of 16% (Ref 1).

In order to provide for the tensile loading at the region of interest, a three-point bending geometry was chosen. Similarly, since current interest in LSP was with leading edge regions of civil engines blades, the test section of TA19 notched simulated blades was designed to approximate a typical airfoil leading edge, with the leading edge thickness of 0.75 mm, as shown in Fig. 2. The stress state of TA19 blades during the actual service was the same as the stress state of bending fatigues of TA19 notched simulated blades shown in Fig. 2. In addition, the fatigue crack propagation direction of TA19 notched simulated blades was perpendicular to the force direction of the blades. The preparation processes of TA19 nrepresents the fatigue stress, which initiallyotched simulated blades were as follows: (1) rough-milling the rectangular outline of the samples from the forged piece; (2) cutting the inclined plane or test section of the samples by a wire electrical discharge machine (EDM); (3) finish-milling the whole test section of the samples; (4) polishing the surface of the samples by emery papers; and (5) cutting a crack started notch with the U notch at the leading edge of TA19 simulated blades by using a EDM, producing a stress free starter notch approximately 0.9 mm deep with a 0.2 mm root radius. Three different LSP processes were used to study the effect of LSP on the anti-FOD fatigue performance of TA19 notched simulated blades. Three different LSP processes were as follows: the as-received material (representing "No-LSP"), LSP with double sides and single spot at each side (representing "LSP-1"), and LSP with double sides and three overlapping spots at each side (representing "LSP-3"). The laser process parameters in detail were presented in Sect. 4.

2.2 Experiment Details

A schematic of TA19 notched simulated blades with LSP is presented in Fig. 3. During the LSP process, an aluminum foil with approximately 0.12 mm thickness was used as an absorbing layer. A water curtain with approximately 1–2 mm thickness was used as a confined layer. In addition, during the LSP process at the top surface, an absorbing wave layer with an aluminum foil and a water curtain was added to the bottom surface of TA19 notched simulated blades. Laser shock wave in the target could spread into an absorbing wave layer, which decreased the amplitude of the reflection wave at the bottom surface of the target and avoided the spall phenomenon inside the target. The thickness of an aluminum foil for the absorbing wave layer was the same as that of an aluminum foil for the absorbing layer. The thickness of a water curtain for the absorbing layer was the same as that of a water curtain for the confined layer. The schematics of TA19 notched simulated blades with two different LSP processes are presented in Fig. 4. During the LSP process, the laser beam or laser spot was fixed, and the platform or the sample was moving. LSP-1 and LSP-3 (Sect. 3) experiments were finished by spraying the top surface first and then spraying the bottom surface. LSP experiments were carried out using a YAG laser with a wavelength of 1064 nm and a pulse width of 15 ns. LSP process parameters of TA19 notched simulated blades were consistent to those at the leading edge of TA19 blades with LSP. The laser process parameters were as follows: a laser energy of 30 J/pulse, a repetition frequency of 1 Hz, square spots of 4 mm × 4 mm, an overlapping ratio of 15% and the moving speed of the moving platform of 3.4 mm/s. Square spots were focused on the top surface of TA19 notched simulated blades using a beam shaping device with a lens and a shaping lens (Ref 18).

The fatigue testing of TA19 notched simulated blades was carried out under three-point bend, constant amplitude loading in a QRG-100 servo-hydraulic fatigue test machine. The support span used in all tests was approximately 80 mm, with

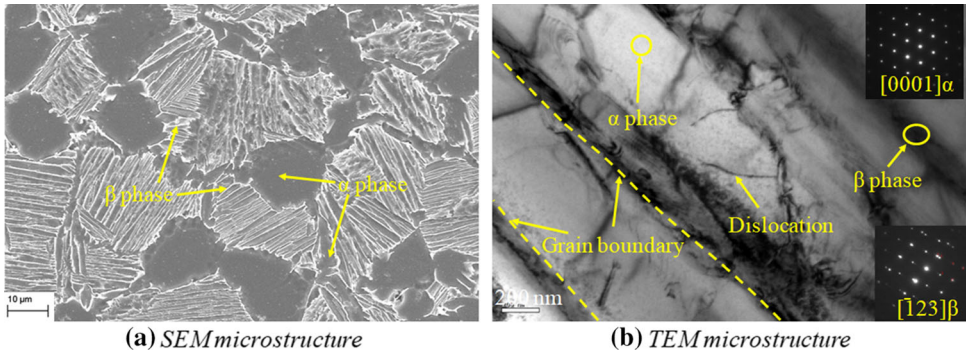

Fig. 1 The microstructure of the as-received TA19 alloy

Table 1 The chemical compositions of the TA19 alloy (wt.%)

Composition	Al	Sn	Zr	Mo	Si	Fe	C	O	Ti
wt.%	5.80	1.88	3.78	1.91	0.08	0.02	0.01	0.11	Balance

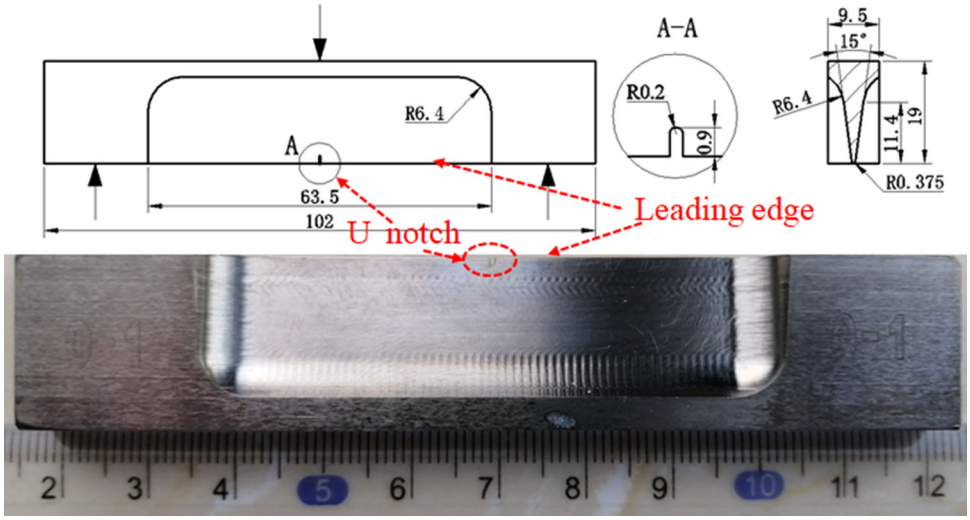

Fig. 2 The dimensions of TA19 notched simulated blades

the support rollers free to rotate and move apart slightly as the sample was loaded. This fixture was available in the ASTM Standard Test Method for Linear-Elastic Plane-Strain Fracture Toughness K_{IC} of Metallic Materials (E399). The test frequency for all tests was the natural frequency of the samples of 94–100 Hz in a laboratory air environment. During the actual service of blades, there were high-cycle/low-cycle fatigue load spectrums with two stress ratios $R = 0.8$ and $R = 0.1$. In this paper, only stress ratio $R = 0.1$ was selected to examine the high-cycle (10^7 cycles) fatigue strength of TA19 notched simulated blades without and with LSP. Figure 5 shows the schematic drawings of the macroscopic fatigue crack propagation paths of TA19 notched simulated blades with two different LSP processes.

The formula for the final calculated fatigue loading force F is as follows:

$$F = \frac{4\sigma \cdot W_z}{L} \quad \text{(Eq 1)}$$

where σ represents the fatigue stress, which initially depends on the yield strength and theoretical stress concentration factor of TA19 notched simulated blades, and $Wz = 134.9$ mm^3 represents the section modulus to the neutral axis/Z axis of TA19 notched simulated blades, and $L = 4\ W \pm 0.2\ W = 72.2$–79.8 mm ($W = 19$ mm represents the width of the samples, as shown in Fig. 2) represents the support span.

2.3 Measured Analysis

The surface morphologies of LSP area with the U notch at the leading edge of TA19 notched simulated blades were measured using a ZYGO NexView optical profiler based on

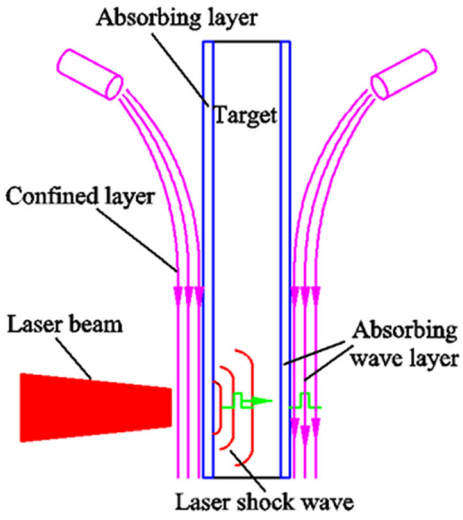

Fig. 3 A schematic of TA19 notched simulated blades with LSP

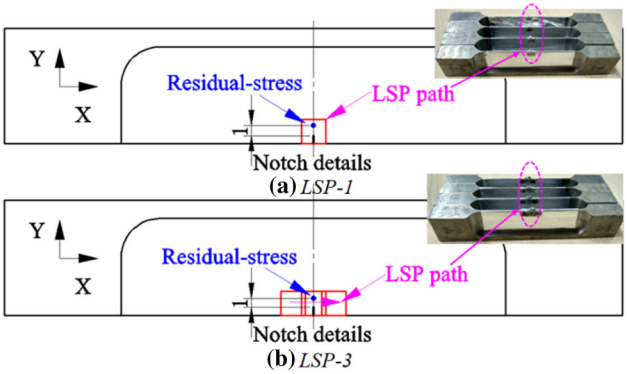

Fig. 4 The schematics of TA19 notched simulated blades with two different LSP processes

the light interference technology. Each measurement was performed for a region of 6 mm × 6 mm. The surface residual stresses at the tip of the U notch at the leading edge of TA19 notched simulated blades with and without LSP were measured via a laboratory x-ray diffraction using the sin2ψ-method, and measured positions are shown in Fig. 4. The diameter of an x-ray beam was approximately 2 mm, and the diffracted *Cu-Kα* characteristic x-rays from hexagonal α-phase {213} plane were detected with a diffraction angle (2θ) of 142°. The measurement positions of residual stresses were 1 mm distance from the tip of the U notch and located at the centerline in the lengthwise direction. Near-surface microstructure at the LSP area with the U notch at the leading edge of TA19 notched simulated blades was characterized using a JEM-2100 transmission electron microscopy (TEM) operated at a voltage of 200 kV. The TEM observation was performed on thin foils, which were first mechanically ground to 50 μm and then perforated using a dimpling and an ion thinning. Fatigue fracture morphology was observed on a ZEISS SUPRA 55 field scanning electron microscope (SEM) at a voltage of 15 kV.

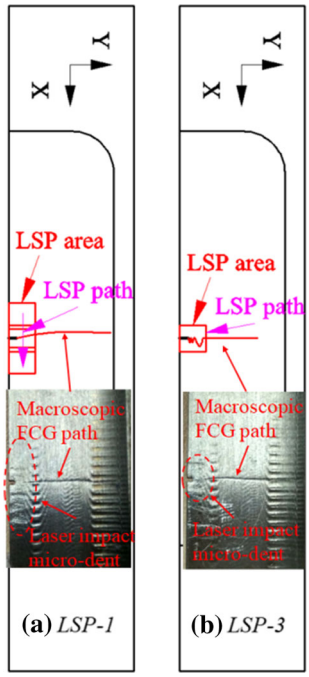

Fig. 5 The schematic drawings of the macroscopic fatigue crack propagation paths of TA19 notched simulated blades with two different LSP processes

3. Results and Discussion

3.1 Surface Morphology

Figure 6 shows 3D surface topographies of TA19 notched simulated blades with two different LSP processes. Micro-dents created by laser shock are shown in Fig. 6. Compared with LSP-3, the depth of the micro-dent induced by LSP-1 is more obviously in the X-direction, as shown in Fig. 6. The reason was that the reference planes of measured depths of micro-dents were the as-received material for LSP-1 and the LSP area for LSP-3. In addition, surface initial conditions at the top and bottom surfaces were the same for all samples. Surface roughnesses parallel to the U notch at the leading edge were similar for TA19 notched simulated blades with LSP-1 and LSP-3 because of single spot used parallel to the U notch for two different LSP processes. An increase in the surface roughness at the top and bottom surfaces may be happened after LSP, which had an attribution to the degradation of fatigue strength (Ref 19). Moreover, the U notches were machined by EDM for TA19 notched simulated blades. Surface roughnesses at the EDM surface of the U notch were the same for TA19 simulated blades with and without LSP. Therefore, based on the above analysis, the surface roughness was not considered in this paper.

Surface profiles of TA19 notched simulated blades with two different LSP processes are presented in Fig. 7. Surface profiles fluctuated greatly because of measuring the edge of the U notch. The width of measured micro-dents was the distance of the intersections of the micro-dents profiles and the reference planes. The depth of measured micro-dents was the distance from the bottom surface to the intersections of the micro-dent profiles and the reference planes. As shown in Fig. 7(a), in the perpendicular to the U notch, LSP treatment induces the micro-

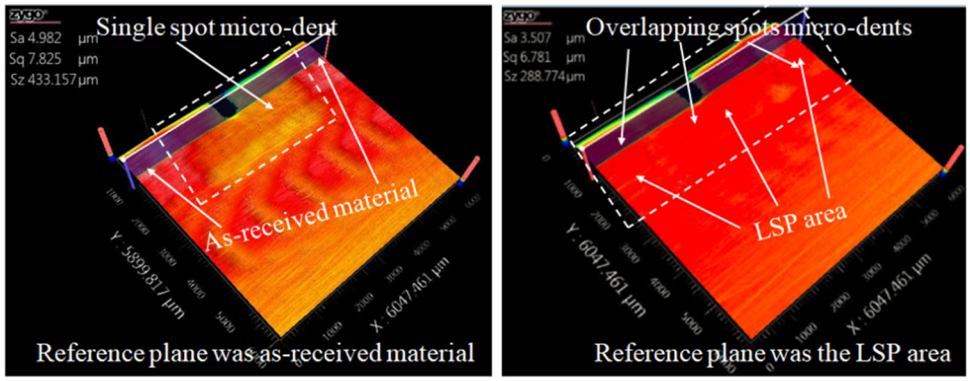

(a) *LSP-1* **(b)** *LSP-3*

Fig. 6 3D surface topographies of TA19 notched simulated blades with two different LSP processes

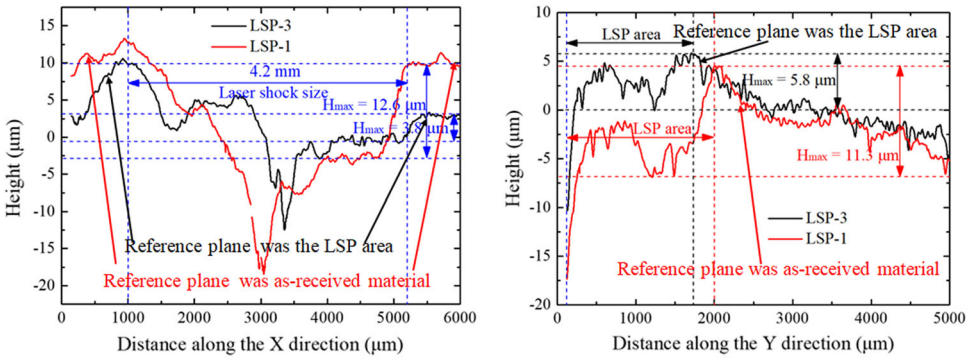

(a) *Perpendicular to the U notch* **(b)** *Parallel to the U notch*

Fig. 7 Surface profiles of TA19 notched simulated blades with two different LSP processes

dent plastic deformation with a laser shock size of 4.2 mm. In addition, the depth of the micro-dent induced by LSP-1 was greater than that of LSP-3. The depths of the micro-dents were 12.6 μm for LSP-1 and 3.8 μm for LSP-3. As shown in Fig. 7(b), in the parallel to the U notch, LSP treatment induces the micro-dent plastic deformation with approximately 2 mm length distancing from the tip of the U notch. In addition, the depth of the micro-dent induced by LSP-1 was also greater than that of LSP-3. The depths of the micro-dents were 11.3 μm for LSP-1 and 5.8 μm for LSP-3. The surface micro-dent plastic deformation induced by LSP caused the generations of compressive residual stresses and refined grains in the surface layer, which were beneficial to improve the fatigue performance of components (Ref 7). Therefore, LSP treatment would be beneficial to improve the fatigue strength of TA19 notched simulated blades.

3.2 Residual Stress

Loading forces were generated along the X-direction during three-point bending fatigue tests of TA19 notched simulated blades. Therefore, residual stress values in the X-direction needed to be increased to enhance the anti-FOD fatigue performance of TA19 notched simulated blades. Then, single spot LSP and three overlapping spots LSP along the X-direction were carried at the leading edge of TA19 notched simulated blades. In addition, LSP-induced maximum compressive residual stresses were located at the surface of TA19 notched simulated blades. Therefore, surface residual stresses in the X-direction were measured and analyzed to study the effect of LSP on the fatigue strength. Residual stress at the tip of the U notch changed at first during the cycle loading. Therefore, only surface residual stresses at the tip of the U notch in the X-direction were analyzed for three different process parameters. Furthermore, three overlapping spots perpendicular to the U notch (in the X-direction) at the leading edge could increase the compressive residual stress values in the X-direction (Sect. 8), which would be beneficial to improve the anti-FOD fatigue performance in the X-direction. Therefore, three overlapping spots and single spot perpendicular to the U notch were used to contrastively study the effect of three different LSP processes on the fatigue strength. Surface residual stresses in the X-direction of TA19 notched simulated blades with three different LSP processes are presented in Fig. 8. Figure 8 shows that LSP induces surface compressive residual stresses in the X-direction at the top and bottom surfaces of TA19 notched simulated blades. This was owing to the severe plastic deformation layer induced by the laser shock wave (Ref 8). From Fig. 8, there are machining stresses of − 133 MPa at the top surface and − 149 MPa at the bottom surface with a shallow affected layer before LSP. After LSP-1, surface compressive residual stresses in the X-direction are − 144 MPa at the top surface and − 168 MPa at the bottom surface. After LSP-3, surface compressive residual stresses in the X-direction are − 185 MPa at the top surface and − 207 MPa at the bottom surface. Compared with No-LSP,

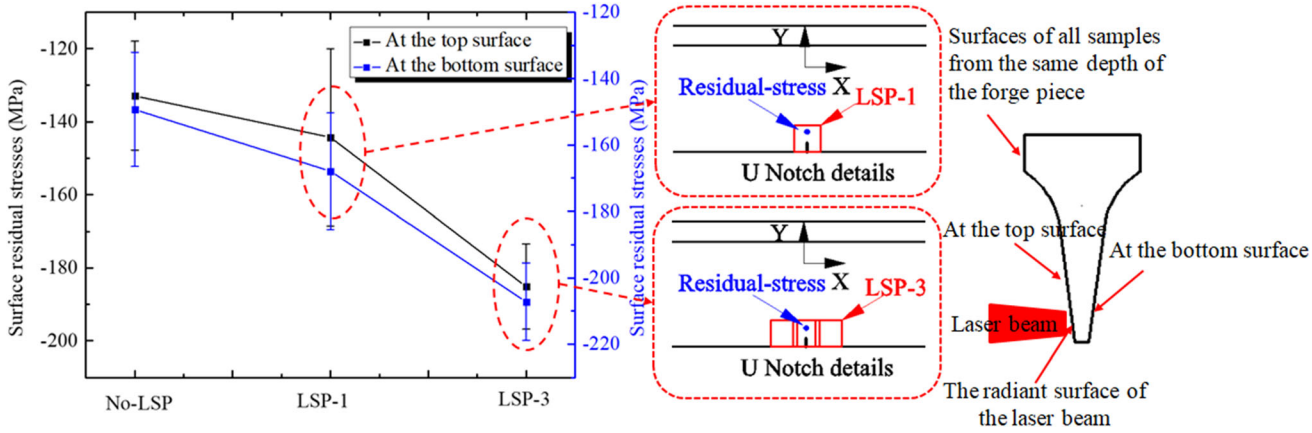

Fig. 8 Surface residual stresses in the X-direction of TA19 notched simulated blades with three different LSP processes

surface compressive residual stresses were increased by 8.3% at the top surface and 12.8% at the bottom surface after LSP-1, and 39.1% at the top surface and 38.9% at the bottom surface after LSP-3. The above results indicated that not high surface compressive residual stresses were induced by LSP, ascribed to the severe plastic deformation/laser deep drawing at the cross section of thin-walled component with LSP (Ref 20). Compressive residual stresses of TA19 notched simulated blades with LSP could prevent the FCI and delay the propagation of fatigue cracks (Ref 4, 12-14). In addition, compared with LSP-1, larger compressive residual stresses induced by LSP-3 could further improve the anti-FOD fatigue performance. Therefore, compressive residual stresses induced by LSP would be beneficial to improve the fatigue strength of TA19 notched simulated blades and high fatigue strength would be obtained by LSP-3.

3.3 Near-Surface Microstructure

More severe micro-plastic deformations were generated in the same depth of near-surface layer of two-phase titanium alloy with the increasement of LSP impact times (Ref 8). In addition, the microstructure evolution mechanism was the same for two-phase titanium alloy with LSP. Therefore, the paper only investigated the near-surface microstructure of TA19 alloy with LSP-1. β phase with body-centered cubic (bcc) crystal structure has high stacking fault energy and more slip systems. α phase with hexagonal close-packed (hcp) crystal structure has low stacking fault energy with only four independent slip systems. Hcp grain needs other deformations to achieve the plastic deformation such as deformation twinning. Therefore, dislocation slips in the β phase and deformation twins in the α phase were generated when the pressure of the laser shock wave exceeded the dynamic yield strength of TA19 alloy. The microstructure plastic deformation mechanism of the β phase was the successive forming of low-density dislocations, high-density dislocations, dislocation tangles, dislocation walls, dislocation cells, sub-grain boundaries and nano-grains. The microstructure plastic deformation mechanism of the α phase was the successive forming of deformation twinning, dislocation lines, dislocation tangles, dislocation cells, sub-grain boundaries and nano-grains (Ref 21). With the increase in the pressure of the laser shock wave, dislocation activities and twins were motivated. And then, high-dense dislocations in the β phase, and high-dense dislocations and deformation twins in the α phase were generated. Therefore, dislocations and twins in the near-surface of TA19 alloy with LSP-1 are formed prior to fatigue tests, as shown in Fig. 9. Compared with No-LSP (Fig. 1b), there are many parallel twins arranged in the α phase after LSP-1, as shown in Fig. 9(a), which is in a good accordance with that observed in the pure titanium with multiple LSP impacts (Ref 22). In addition, dislocation tangles, dislocation cells and planar dislocations can also be observed in the α phase, as shown in Fig. 9(b). The change from high-dense dislocations to planar dislocations was consistent with the observation of Lainé (Ref 23). The reason was that once twins were no longer able to accommodate the plastic strain, dislocation slips were activated and high-dense dislocations were generated in the near grain boundaries and twin boundaries, which had high strain and easily acted as dislocation nucleation sites (Ref 24). Besides, high-dense dislocations in the β phase were caused by the higher dislocation mobility as a result of LSP-1. Therefore, complex arrays of dislocations are observed in the β phase, as shown in Fig. 9(c). Meanwhile, the bending dislocation lines and high distortions are also formed in the β phase, as shown in Fig. 9(c). These were owing to the severe plastic deformation in the β phase. More importantly, there are large numbers of surface nano-grains in the α and β phases, as shown in Fig. 9(d).

According to the formulation for the relationship between the dislocation density and the alloy's fatigue strength: $\sigma_f = \sigma_0 + \kappa\left(d_{fp}\right)^{-1/2} + \alpha G b \rho^{1/2}$ (Ref 25, 26), the highest work hardening and the fatigue strength occurred in the near-surface region of TA19 alloy with LSP-1 because of high-density dislocations, twins and surface nano-grains induced by the plastic strain. Therefore, refined grains induced by LSP-1 would be beneficial to improve the fatigue performance of the near-α titanium alloy (Ref 3), such as the fatigue strength of TA19 notched simulated blades.

3.4 Fatigue Strength

The same initial surface conditions were obtained for TA19 notched simulated blades with three different LSP conditions due to the machining process. Three-point bending fatigue strengths of TA19 notched simulated blades with three different LSP processes are presented in Fig. 10. For three-point bending fatigue tests, Ganesh et al. (Ref 27) have reported that fatigue lives could be improved by resorting to LSP. For notched simulated blades, fatigue lives could also be improved by

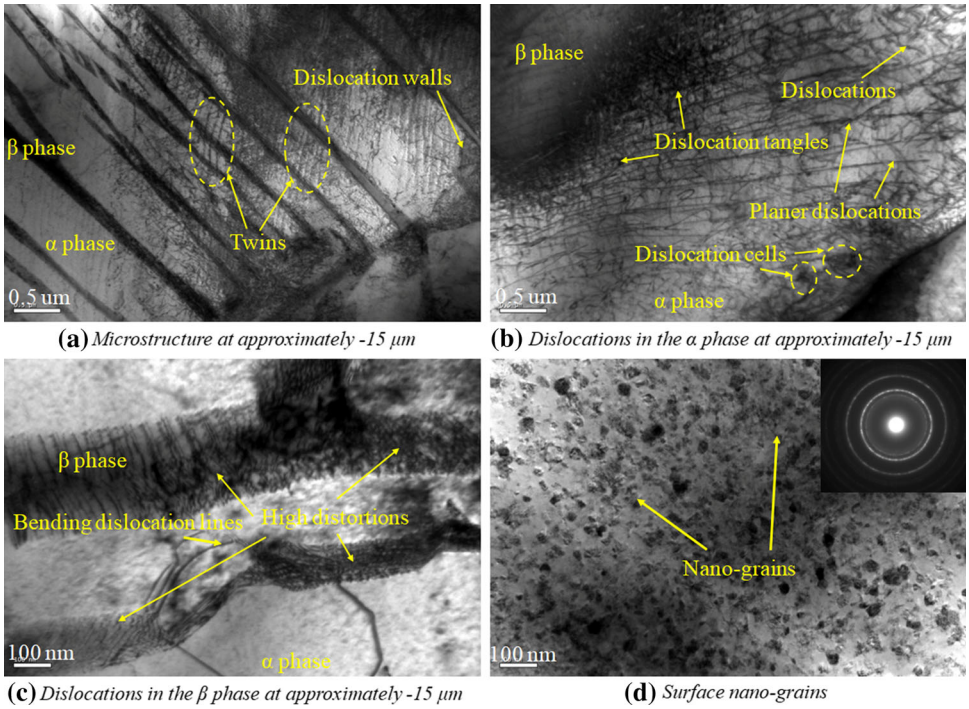

Fig. 9 Near-surface microstructures of TA19 alloy with LSP-1

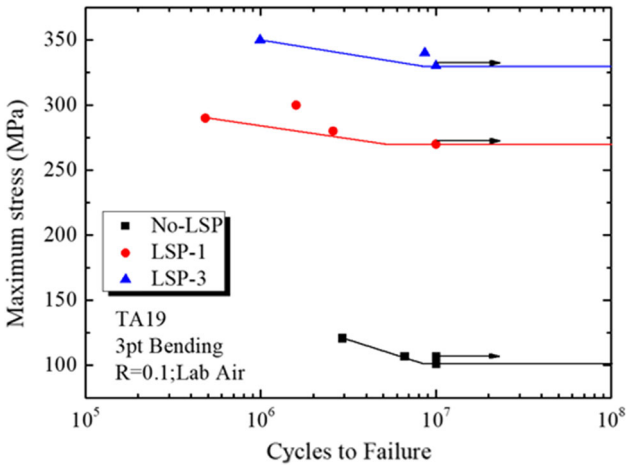

Fig. 10 Three-point bending fatigue strengths of TA19 notched simulated blades with three different LSP processes

double-sided LSP (Ref 4, 9, 12). In this study, compared with No-LSP, an increase in fatigue strengths of TA19 notched simulated blades is observed for two LSP processes and the best improvement is given by LSP-3, as shown in Fig. 10. The results have also been reported by Spanrad (Ref 15). The results may be came from the creations of near-surface microstructure changes (Sect. 3.3) and compressive residual stresses (Sect. 3.2) (Ref 9), and surface compressive residual stress values after LSP-3 were higher than those after LSP-1 (Fig. 8). It can be seen from Fig. 10 that LSP-3 lasts approximately 340 MPa to failure corresponding to 218% improvement with respect to No-LSP (approximately 107 MPa to failure), while LSP-1 lasts approximately 280 MPa to failure corresponding to 162% improvement with respect to No-LSP (approximately 107 MPa to failure).

Fatigue strength was associated with the accumulation of the plastic deformation in the near-surface region. The plastic deformation gave rise to the FCI after several loading cycles (Ref 28). LSP-induced compressive residual stresses (Sect. 8) could reduce the plastic deformation caused by the external force in the near-surface region, which decreased the stress intensity factor ΔK and delayed the FCG rate da/dN (Ref 29). The relationship between compressive residual stresses and fatigue lives has been reported by Dorman et al. (Ref 30). The results indicated that fatigue cracks were always initiated in the regions with the maximum tensile stress induced by the machining stress and inhibited by the compressive residual stress. Furthermore, refined grains (Sect. 9) in the near-surface region could block the dislocation slips induced by the plastic deformation, which improved the resistances of FCI and FCG in vulnerable regions (Ref 31). In summary, both presences of compressive residual stresses and refined grains resulted in a significant improvement in the fatigue strength of TA19 notched simulated blades and high fatigue strength was obtained by LSP-3 because of high compressive residual stresses.

3.5 Fatigue Fracture Morphology

The fatigue fracture failure was shown by macroscopic fatigue cracks at the surface of fatigue samples. In addition, macroscopic fatigue crack propagation paths at the surface indirectly displayed the fatigue behavior. Therefore, macroscopic fatigue crack propagation paths of TA19 notched simulated blades with three different LSP processes are contrastively studied to analyze the fatigue behavior, as shown in Fig. 11. As shown, it was remarkably different for TA19 notched simulated blades with and without LSP to form the fatigue crack propagation paths. When notched simulated

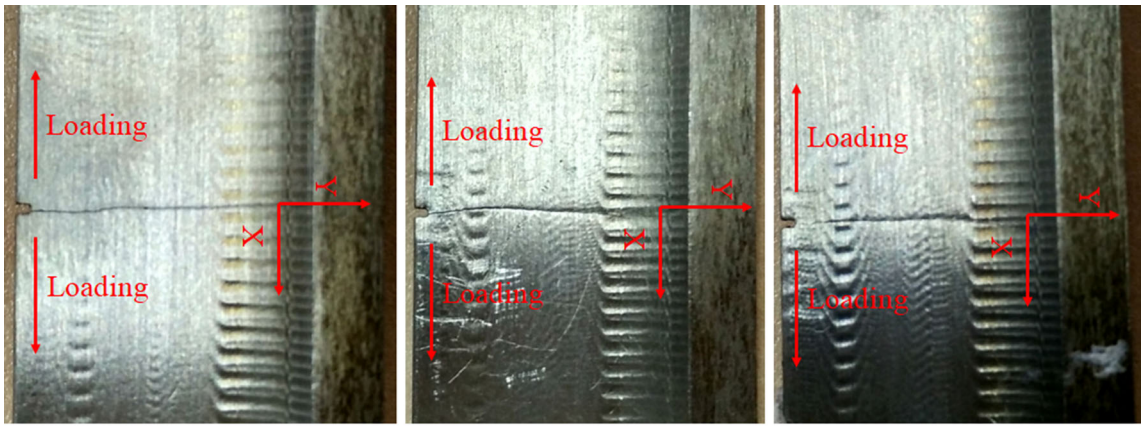

Fig. 11 Macroscopic fatigue crack propagation paths of TA19 notched simulated blades with three different LSP processes

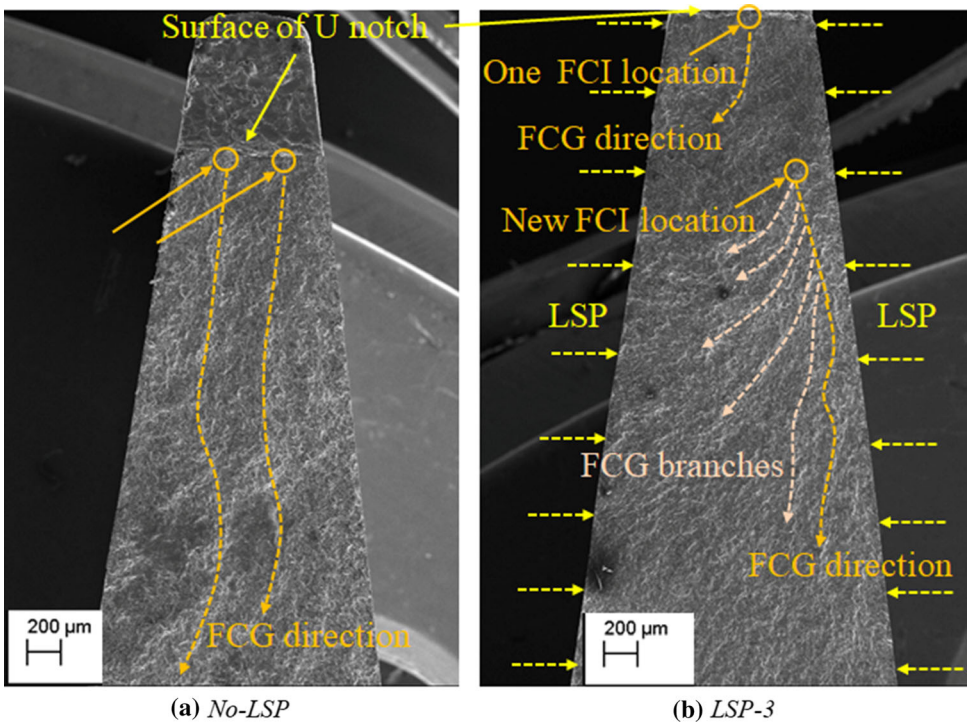

Fig. 12 Macroscopic fatigue fracture morphologies of TA19 notched simulated blades without and with LSP

blades were pulled by the external loading, fatigue cracks initiated and propagated along the orthogonal direction of the external loading. Therefore, the macroscopic fatigue crack propagation path of TA19 notched simulated blades with No-LSP is parallel to the U notch and straightforward, as shown in Fig. 11(a). However, after LSP, combined actions of compressive residual stresses and refined grains made the fatigue micro-crack easily propagate into the adjacent grains. Therefore, the macroscopic fatigue crack propagation path of TA19 notched simulated blades with LSP-1 inclines to the U notch, as shown in Fig. 11(b). When three overlapping spots were carried along the X-direction, an increase in compressive residual stresses in the X-direction was generated, which would make the fatigue micro-crack hardly propagate. Then, the macroscopic fatigue crack propagation path of TA19 notched simulated blades with LSP-3 twists to the U notch, as shown in Fig. 11(c). Inclined and twisty propagation paths could consume much plastic deformation energy, which delayed the FCG rate. As a result, LSP treatment improved the fatigue strength of TA19 notched simulated blades through compressive residual stresses and refined grains.

Macroscopic fatigue fracture morphologies of TA19 notched simulated blades without and with LSP are presented in Fig. 12. For the same surface roughnesses of the U notch without and with LSP, FCI locations in fracture surfaces are changed from two locations of No-LSP to one location of LSP-3, as shown in Fig. 12. On the one hand, the results indicated that LSP could strengthen the metal surface and suppress the

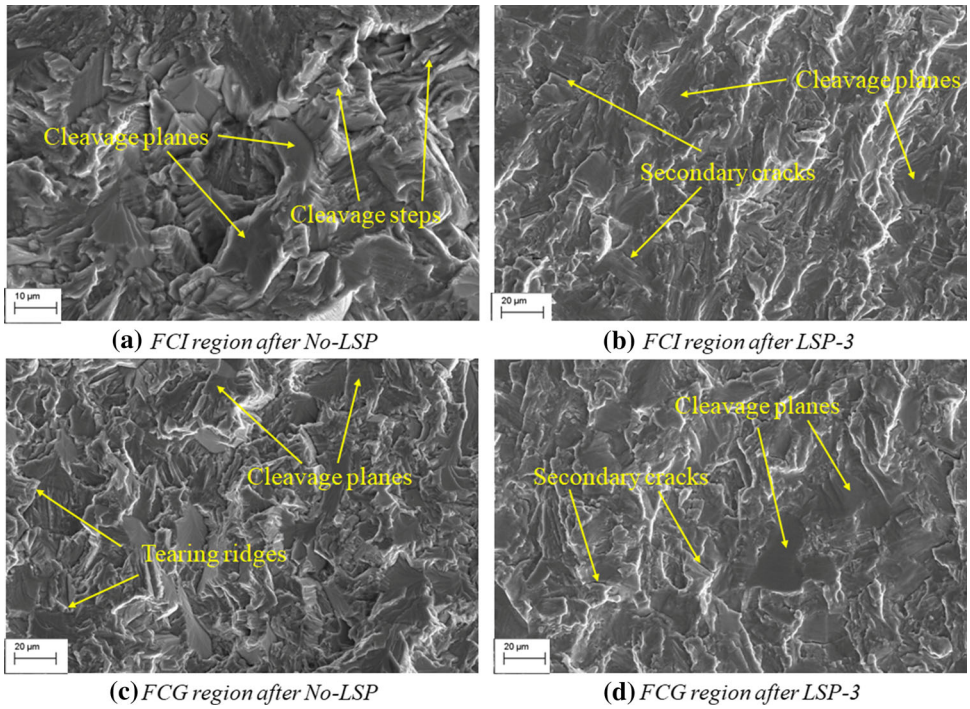

Fig. 13 Microscopic fatigue fracture morphologies of TA19 notched simulated blades without and with LSP

crack initiation. On the other hand, fatigue cracks originated in the local micro-region with the strain concentration. Compared with No-LSP, LSP-induced surface compressive residual stresses decreased the strain concentration at the EDM surface of the U notch. Therefore, FCI positions of LSP are reduced to one site, as shown in Fig. 12.

With the increase in cycle numbers, a large number of slip bands are formed and then fatigue cracks are generated along the direction of slip bands, as shown in Fig. 12. For TA19 notched simulated blades with No-LSP, the density of slip bands increased and propagated along the orthogonal direction of the external loading during the cyclic loading, which started from two FCI locations at the same time. Therefore, there are two continuous FCG lines in the fatigue fracture morphology, as shown in Fig. 12(a). However, refined grains were generated at the whole cross section of TA19 notched simulated blades with LSP (Sect. 9). Therefore, slip bands were easy to propagate into the adjacent grains during the cyclic loading. These might cause the termination of the main FCG line and generations of a new FCI location and a new FCG line with many FCG branches. As a result, there are two discontinuous FCG lines and many FCG branches in the fatigue fracture morphology, as shown in Fig. 12(b). A new FCI location and a new FCG line with many FCG branches could consume much plastic deformation energy, which delayed the FCG rate. In summary, LSP treatment effectively improved the FCI life and FCG rate of TA19 notched simulated blades through compressive residual stresses and refined grains.

Microscopic fatigue fracture morphologies of TA19 notched simulated blades without and with LSP are presented in Fig. 13. In a hexagonal crystal of α-Ti, the cleavage plane is the {0001} plane. In general, microcracks initiate along the {0001} cleavage planes (Ref 22). Moreover, the preferable slip plane of TA19 is also the {0001} plane. Therefore, localized slips of TA19 notched simulated blades before and after LSP occur along the cleavage planes under a certain grain orientation, strain and stress (Ref 32). Hence, cleavage planes, cleavage steps and tearing ridges can be seen in the FCI and FCG regions before and after LSP, as shown in Fig. 13. The similar results have been reported in Ref. (33). Besides, compared with No-LSP, secondary cracks are generated in the FCI and FCG regions after LSP-3, as shown in Fig. 13. The same results have been reported in Ref. 7, 8. Secondary cracks needed to consume much plastic deformation energy (Ref 30). Moreover, dislocation tangles, dislocation walls and dislocation cells in the near-surface region induced by LSP (Sect. 9) hindered the dislocation slips and plastic deformation of TA19 notched simulated blades during the fatigue tests. As a result, LSP effectively prevented the FCI and reduced the FCG rate of TA19 notched simulated blades through refined grains, consistent with (Ref. 34, 35).

3.6 Fatigue Strengthening Mechanism

The studies from Fig. 6 to 13 were about surface integrity, fatigue strength and fatigue fracture morphologies. The results indicated that fatigue strengthening mechanism of TA19 notched simulated blades was the comprehensive action of compressive residual stresses and refined grains induced by LSP. The fatigue strengthening mechanism could be concluded as follows:

(1) In the FCI stage, compressive residual stresses played a very important role on the fatigue strength owing to the compressive residual stress counteracting a part of the tensile stress (Ref 36). Compressive residual stresses (section "Residual Stress") induced by LSP acted as a shield and lowered the stress intensity during fatigue tests, which compelled or at least delayed the initiation of fatigue cracks (Fig. 12). The similar has been reported in Ref. (15). According to the formula for the stress intensity factor: $\Delta K = y\Delta\sigma\sqrt{\pi a} \geq \Delta K_{IC}$ (Ref 37), LSP-induced compressive residual stresses decreased the stress

intensity factor ΔK, which was less than the threshold value ΔK_{IC} of the fatigue crack. Therefore, LSP-induced surface compressive residual stresses decreased the strain concentration at the EDM surface of the U notch. And then, FCI positions were reduced from two sites to one site (Fig. 12). Besides the positive contribution of compressive residual stress for fatigue performance, the microstructural evolution induced by LSP also had an important influence. LSP-induced refined grains (Sect. 9) in the surface layer, with fatigue cracks initiated, bring more grain boundaries which can improve the resistance for slip deformation, restrain the generation of slip bands and increase the grain boundary resistance for crack extension. Therefore, fatigue cracks were very hard to initiate in the surface layer after LSP, which prolonged the FCI life. It caused the termination of the main FCG line and generations of a new FCI location and a new FCG line with many FCG branches. As a result, there were two discontinuous FCG lines and many FCG branches in the fatigue fracture morphology (Fig. 12).

(2) In the FCG stage, compressive residual stresses could improve the threshold value of FCG. According to the formula for the relation between the residual stress and the FCG rate: $\frac{da}{dN} = \frac{C(\Delta K)^m}{[(1-R)K-\Delta K]}$ (Ref 38), LSP-induced compressive residual stresses decreased the practical efficient stress during fatigue tests, which reduced the FCG rate. Meanwhile, compressive residual stresses (Sect. 8) increased the closing force of microscopic cracks, which retarded the propagation of fatigue cracks. Besides, when a fatigue crack was initiated, under the blocking of tremendous refined grain boundaries in the surface layer induced by LSP, FCG rate would be decreased. A new FCI location and a new FCG line with many FCG branches could consume much plastic deformation energy, which delayed the FCG rate (Fig. 12). And then, some fatigue cracks were compelled to swerve (Fig. 11b and c) or stopped to extend (Fig. 12(b)). Therefore, many secondary cracks were generated in the fatigue fracture morphology (Fig. 13b and d). Therefore, refined grains were the main strengthening factor when compressive residual stresses were relaxed in the later stage of fatigue tests.

4. Conclusions

The surface integrity and fatigue strength of TA19 notched simulated blades without and with LSP were investigated. The fatigue strengthening mechanism of TA19 notched simulated blades with LSP was revealed. The following conclusions were drawn:

(1) LSP induced the micro-dent plastic deformation at the U notch area of the leading edge. It caused the surface compressive residual stress in the X-direction and surface nano-grains in the α and β phases. Compressive residual stresses decreased the stress intensity factor ΔK and increased the closing force of microscopic cracks. Refined grains in the near-surface region could block the dislocation slips induced by the plastic deformation, which improved the resistances of FCI and FCG in vulnerable regions. Then, compared with No-LSP, fatigue strengths of TA19 notched simulated blades were increased by 162% for LSP-1 and 218% for LSP-3.

(2) Refined grains brought in more grain boundaries, which could improve the slip resistance, restrain the generation of slip bands and increase the grain boundary resistance against FCG. In addition, an increase in compressive residual stresses would make the fatigue micro-crack hardly propagate. Therefore, the macroscopic fatigue crack propagation path of TA19 notched simulated blades inclined to the U notch after LSP-1 and twisted to the U notch after LSP-3. Many secondary cracks were generated after LSP.

(3) LSP-induced surface compressive residual stresses decreased the strain concentration at the EDM surface of the U notch. FCI locations in the fracture surfaces were changed from two locations of No-LSP to one location of LSP-3. In addition, slip bands were easy to propagate into the adjacent grains by refined grains during the cyclic loading. These might cause the termination of the main FCG line and generations of a new FCI location and a new FCG line with many FCG branches.

Acknowledgments

This research was supported by the National Natural Science Foundation of China (No. 51875542, 51975084), Civil Aircraft Research Projects (No. MJ-2016-F-16), General assembly pre-research project (No. KZ011708) and Aviation Fund (20185425009).

References

1. D.G. Li, K. Wang, Z.B. Yan, Y. Cao, R.D.K. Misra, R.L. Xin et al., Evolution of Microstructure and Tensile Properties During the Three-Stage Heat Treatment of TA19 Titanium Alloy, *Mater. Sci. Eng. A*, 2018, **716**(14), p 157–164
2. R.R. Boyer, An Overview on the Use of Titanium in the Aerospace Industry, *Mater. Sci. Eng. A*, 1996, **213**(1–2), p 103–114
3. W.J. Jia, Q. Hong, H.Z. Zhao, L. Li, and D. Han, Effect of Laser Shock Peening on the Mechanical Properties of a Near-α Titanium Alloy, *Mater. Sci. Eng. A*, 2014, **606**(12), p 354–359
4. B. Lin, C. Lupton, S. Spanrad, J. Schofield, and J. Tong, Fatigue Crack Growth in Laser-Shock-Peened Ti-6Al-4 V Aerofoil Specimens due to Foreign Object Damage, *Int. J. Fatigue*, 2014, **59**, p 23–33
5. T. Nicholas, Critical Issues in High Cycle Fatigue, *Int. J. Fatigue*, 1999, **21**(1), p 221–231
6. J.J. Ruschau, T. Nicholas, and S.R. Thompson, Influence of Foreign Object Damage (FOD) on the Fatigue Life of Simulated Ti6Al4 V Airfoils, *Int. J. Impact Eng.*, 2001, **25**(3), p 233–250
7. S.K. Zou, J.F. Wu, Y.K. Zhang, S.L. Gong, G.F. Sun, Z.H. Ni et al., Surface Integrity and Fatigue Lives of Ti17 Compressor Blades Subjected to Laser Shock Peening with Square Spots, *Surf. Coat. Technol.*, 2018, **347**, p 398–406
8. X.F. Nie, W.F. He, S.L. Zang, X.D. Wang, and J. Zhao, Effect Study and Application to Improve High Cycle Fatigue Resistance of TC11 Titanium Alloy by Laser Shock Peening with Multiple Impacts, *Surf. Coat. Technol.*, 2014, **253**, p 68–75
9. J.F. Wu, S.K. Zou, Y.K. Zhang, G.F. Sun, Z.H. Ni, Z.G. Che et al., FOD Resistance of the Simulator Samples of TC17 Blades Leading Edges with Laser Shock Processing, *Rare Metal Mater. Eng.*, 2018, **47**(11), p 113–118
10. R. Hall, J. Byrne, T. Zhao, and J. Tong, Influence of Foreign Object Damage on Fatigue Crack Growth of Gas Turbine Aerofoils Under Complex Loading Conditions, *Fatigue Fract. Eng. M*, 2008, **31**(5), p 386–397
11. J. Ding, R.F. Hall, J. Byrne, and J. Tong, Fatigue crack Growth from Foreign Object Damage Under Combined Low and High Cycle Loading. Part I: Experimental Studies, *Int. J. Fatigue*, 2007, **29**(7), p 1339–1349

12. S. Zabeen, M. Preuss, and P.J. Withers, Evolution of a Laser Shock Peened Residual Stress Field Locally with Foreign Object Damage And Subsequent Fatigue Crack Growth, *Acta Mater.*, 2015, **83**, p 216–226
13. J.J. Ruschau, R. John, S.R. Thompson, and T. Nicholas, Fatigue Crack Nucleation and Growth Rate Behavior of Laser Shock Peened Titanium, *Int. J. Fatigue*, 1999, **21**(1), p S199–S209
14. J.J. Ruschau, R. John, S.R. Thompson, and T. Nicholas, Fatigue Crack Growth Rate Characteristics of Laser Shock Peened Ti-6AI-4 V, *J. Eng. Mater. Technol.*, 1999, **121**(3), p 321–329
15. S. Spanrad and J. Tong, Characterisation of Foreign Object Damage (FOD) and Early Fatigue Crack Growth in Laser Shock Peened Ti-6Al-4 V Aerofoil Specimens, *Mater. Sci. Eng. A*, 2011, **528**(4–5), p 2128–2136
16. S.H. Luo, X.F. Nie, L.C. Zhou, Y.H. Li, and W.F. He, High Cycle Fatigue Performance in Laser Shock Peened TC4 Titanium Alloys Subjected to Foreign Object Damage, *J. Mater. Eng. Perform.*, 2018, **27**, p 1466–1474
17. S. Zabeen, M. Preuss, and P.J. Withers, Residual Stresses Caused by Head-on and 45° Foreign Object Damage for a Laser Shock Peened Ti-6Al-4 V Alloy Aerofoil, *Mater. Sci. Eng. A*, 2013, **560**(10), p 518–527
18. Z.W. Cao, H.Y. Xu, S.K. Zou, and Z.G. Che, Investigation of Surface Integrity on TC17 Titanium Alloy Treated by Square-spot Laser Shock Peening, *Chin. J. Aeronaut.*, 2012, **25**(4), p 650–656
19. X.C. Zhang, Y.K. Zhang, J.Z. Lu, F.Z. Xuan, Z.D. Wang, and S.T. Tu, Improvement of Fatigue Life of Ti–6Al–4 V Alloy by Laser Shock Peening, *Mater. Sci. Eng. A*, 2010, **527**(15), p 3411–3415
20. Y.X. Hu, X.X. Xu, Z.Q. Yao, and J. Hu, Laser Peen Forming Induced Two Way Bending of Thin Sheet Metals and Its Mechanisms, *J. Appl. Phys.*, 2010, **108**(7), p 073117-1–073117-7
21. X.D. Ren, W.F. Zhou, F.F. Liu, Y.P. Ren, S.Q. Yuan, N.F. Ren et al., Microstructure Evolution and Grain Refinement of Ti-6Al-4 V Alloy by Laser Shock Processing, *Appl. Surf. Sci.*, 2016, **363**(15), p 44–49
22. J.Z. Lu, L.J. Wu, G.F. Sun, K.Y. Luo, Y.K. Zhang, J. Cai et al., Microstructural Response and Grain Refinement Mechanism of Commercially Pure Titanium Subjected to Multiple Laser Shock Peening Impacts, *Acta Mater.*, 2017, **127**(1), p 252–266
23. S.J. Lainé, K.M. Knowles, P.J. Doorbar, R.D. Cutts, and D. Rugg, Microstructural Characterization of Metallic Shot Peened and Laser Shock Peened Ti-6Al-4 V, *Acta Mater.*, 2017, **123**(15), p 350–361
24. H. Zhang, Z.C. Ren, J. Liu, J.Y. Zhao, Z.K. Liu, D. Lin et al., Microstructure Evolution and Electroplasticity in Ti64 Subjected to Electropulsing-Assisted Laser Shock Peening, *J. Alloys Compd.*, 2019, **802**(25), p 573–582
25. H.K. Kim and W.J. Kim, Microstructural Instability and Strength of an AZ31 Mg Alloy After Severe Plastic Deformation, *Mater. Sci. Eng. A*, 2004, **385**(1–2), p 300–308
26. S.H. Luo, W.F. He, L.C. Zhou, X.F. Nie, and Y.H. Li, Aluminizing Mechanism on a Nickel-Based Alloy with Surface Nanostructure Produced by Laser Shock Peening and Its Effect on Fatigue Strength, *Surf. Coat. Technol.*, 2018, **342**(25), p 29–36
27. P. Ganesh, R. Sundar, H. Kumar, R. Kaul, K. Ranganathan, P. Hedaoo et al., Studies on Fatigue Life Enhancement of Pre-Fatigued Spring Steel Specimens Using Laser Shock Peening, *Mater. Des.*, 2014, **54**, p 734–741
28. I. Bantounas, D. Dye, and T.C. Lindley, The Role of Microtexture on the Faceted Fracture Morphology in Ti-6Al-4V Subjected to High-Cycle Fatigue, *Acta Mater.*, 2010, **58**(11), p 3908–3918
29. L. Zhang, J.Z. Lu, Y.K. Zhang, K.Y. Luo, J.W. Zhong, C.Y. Cui et al., Effects of Different Shocked Paths on Fatigue Property of 7050-T7451 Aluminum Alloy During Two-Sided Laser Shock Processing, *Mater. Des.*, 2011, **32**(2), p 480–486
30. M. Dorman, M.B. Toparli, N. Smyth, A. Cini, M.E. Fitzpatrick, and P.E. Irving, Effect of Laser Shock Peening on Residual Stress and Fatigue Life of clad 2024 Aluminum Sheet Containing Scribe Defects, *Mater. Sci. Eng. A*, 2012, **548**(30), p 142–151
31. S. Huang, Y. Zhu, W. Guo, P. Peng, and X.G. Diao, Impact Toughness and Microstructural Response of Ti-17 Titanium Alloy Subjected to Laser Shock Peening, *Surf. Coat. Technol.*, 2017, **327**, p 32–41
32. R.S. James, A.C. Martin, R.B. Thomas, and C.J. Boehlert, Analysis of Slip Transfer and Deformation Behavior Across the α/β Interface in Ti-5Al-2.5Sn (wt.%) with an Equiaxed Microstructure, *Mater. Sci. Eng. A*, 2012, **552**(30), p 61–68
33. R.J. Sun, L.H. Li, W. Guo, P. Peng, T.G. Zhai, Z.G. Che et al., Laser Shock Peening Induced Fatigue Crack Retardation in Ti-17 Titanium Alloy, *Mater. Sci. Eng. A*, 2018, **737**, p 94–104
34. A. Pineau and S.D. Antolovich, High Temperature Fatigue of Nickel-Base Superalloys—A Review with Special Emphasis on Deformation Modes and Oxidation, *Eng. Fail. Anal.*, 2009, **16**(8), p 2668–2697
35. J.T. Wang, Y.K. Zhang, J.F. Chen, J.Y. Zhou, K.Y. Luo, W.S. Tan et al., Effect of Laser Shock Peening on the High-Temperature Fatigue Performance of 7075 Aluminum Alloy, *Mater. Sci. Eng. A*, 2017, **704**(17), p 459–468
36. X.Q. Zhang, H. Li, X.L. Yu, Y. Zhou, S.W. Duan, S.Z. Li et al., Investigation on Effect of Laser Shock Processing on Fatigue Crack Initiation and Its Growth in Aluminum Alloy Plate, *Mater. Des.*, 2015, **65**, p 425–431
37. Y.F. Jiang, B. Ji, X.D. Gan, Ch Hua, X. Li, and H. Zhu, Study on the Effect of Laser Peening with Different Power Densities on Fatigue Life of Fastener Hole, *Opt. Laser Technol.*, 2018, **106**, p 311–320
38. R.G. Forman, V.E. Kearney, and R.M. Engle, Numerical Analysis of Crack Propagation in Cyclic-Loaded Structures, *J. Fluid Eng. Trans. ASME*, 1967, **89**(3), p 459–463